micromachines

MDPI

Article

Polarization-Independent Terahertz Reconfigurable Multifunctional Liquid-Crystal Coding Metasurface Based on NSGA-II Topological Optimization

Chenwenji Wang, Yueyang Jing, Jiaqi Luan, Zhiming Wang, Yuanjian Liu * and Peili Li *

College of Electronic and Optical Engineering & College of Flexible Electronics (Future Technology), Nanjing University of Posts and Telecommunications, Nanjing 210023, China; wangcwj@njupt.edu.cn (C.W.)
* Correspondence: liuyj@njupt.edu.cn (Y.L.); lipl@njupt.edu.cn (P.L.); Tel.: +86-13951901292 (Y.L.); +86-18951896687 (P.L.)

Abstract

Terahertz (THz) waves show great potential in high-speed communications and radar detection, and achieving their efficient and flexible manipulation is a current research hotspot. In this work, a polarization-independent THz reconfigurable, multifunctional liquid crystal (LC) coding metasurface based on topological optimization is proposed. First, the metasurface unit is optimized using the non-dominated sorting genetic algorithm II (NSGA-II) for multi-objective topology optimization. By exploiting the electrically tunable refractive index properties of LC, the metasurface unit enables polarization-independent 2-bit coding at 0.56 THz. Subsequently, the NSGA-II and particle swarm optimization (PSO) are employed to inversely design the array arrangement of the metasurface, achieving beam steering and radar cross section (RCS) reduction functionalities. The simulation results show that the proposed 2-bit coding metasurface can achieve polarization-independent single- and multi-beam steering with arbitrary elevation angles within ±30° and azimuth angles spanning the full 360° range. For multi-beam steering, the elevation and azimuth angles of each beam can be independently controlled. In addition, RCS reduction exceeding 10 dB is achieved over a broad frequency range of 0.128–0.710 THz, corresponding to a fractional bandwidth of 138.90%. Therefore, the proposed THz LC metasurface can realize flexible control of reconfigurable functions and holds promising application prospects in THz communications and phased-array radar.

Keywords: coding metasurfaces; polarization-independent; terahertz; topological optimization; multifunctional

Check for updates

Academic Editor: Yuan-Fong Chou Chau

Received: 25 October 2026
Revised: 25 November 2026
Accepted: 27 November 2026
Published: 29 November 2026

Copyright: © 2026 by the authors. Licensee MDPI, Basel, Switzerland. This article is an open access article distributed under the terms and conditions of the Creative Commons Attribution (CC BY) license.

1. Introduction

Metasurfaces, as artificial subwavelength materials, possess powerful capabilities in manipulating incident electromagnetic waves. They offer advantages such as thin thickness, low loss, small volume, and easy integration [1], exhibiting significant potential in THz wavefront manipulation. Digital coding metasurfaces which discretize continuous electromagnetic responses into digital coding sequences, significantly enhance the computational efficiency of metasurface arrays. Building on this, the integration of tunable materials into coding metasurfaces provides an innovative approach for dynamic THz beam control. Under external control, such metasurfaces enable flexible reconfiguration of THz beams, demonstrating high tunability and reconfigurability, and have become one of the mainstream solutions for coding metasurface design in the THz band. Commonly used tunable materials include LC, graphene, vanadium dioxide (VO_2), and Dirac semimetals.

In 2019, Zhao et al. [2] designed a voltage-tunable liquid crystal digital metasurface, achieving beam deflection with a steering elevation angle of 27° and radar cross-section (RCS) reduction in the 51–56 GHz range; in 2020, Xiao et al. [3] proposed a graphene-based terahertz beam deflection coding metasurface, where changing the Fermi level of graphene at 1.9 THz enabled beam deflection with a deflection angle of 19° and azimuth angles of 0°, 90°, 180°, and 270° on a 2-bit coding unit; in 2021, Liu et al. [4] designed an asymmetric resonant "C"-shaped ring liquid-crystal metasurface that achieved 1-bit coding and dual-beam deflection within an elevation angle range of 31.9° at 0.408 THz; in 2023, Lv et al. [5] proposed a VO_2-based multifunctional terahertz programmable metasurface that achieved 1-bit (0011) coding and dual-beam shaping within a 43° range in the 0.735–0.965 THz band, and in the same year, Zhang et al. [6] proposed a tunable multi-bit coding metasurface based on tuning the Fermi level of a Dirac semimetal, achieving 3-bit coding and RCS reduction at 1.88 THz; in 2024, Zhang et al. [7] proposed a terahertz thin liquid crystal (LC) coding metasurface based on topology optimization design, achieving 2-bit coding and beam manipulation within an elevation angle range of 30° at 0.394 THz; and in 2025, Luan et al. [8] proposed a Dirac semimetal-based multifunctional reconfigurable terahertz coding metasurface, achieving 2-bit coding and beam manipulation within an elevation angle range of 40° and an azimuth angle range of 360° at 1.95 THz.

In summary, by introducing tunable materials, metasurfaces can achieve reconfigurability between different functions. However, with the increasing complexity of functional requirements, the structural design of metasurface units and array arrangements faces significant challenges. Topology optimization, which discretizes the unit into pixel grids and utilizes optimization algorithms for inverse design, can effectively improve design freedom and efficiency. It has been applied to the design of broadband absorbers [9], polarization converters [10], and multi-bit coding units [11]. However, existing topology optimization approaches predominantly employ single-objective optimization algorithms, which struggle to address the conflicts among multiple objectives.

Based on the above analysis, using LC as the tunable material, we propose a polarization-independent LC 2-bit coding metasurface based on the combination of the NSGA-II multi-objective optimization algorithm and topology optimization. Unlike previous single-function frameworks, this design achieves both dynamic multi-beam steering and ultra-broadband RCS reduction (with a fractional bandwidth of 138.90%), overcoming the limitations of narrow bandwidths and polarization sensitivity. First, an LC coding unit with polarization-independent 2-bit phase states is developed through multi-objective topology optimization using the non-dominated sorting genetic algorithm II (NSGA-II). At the target frequency of 0.56 THz, the optimized unit naturally provides reconfigurable 2-bit phase responses with an average phase difference of 90°. Subsequently, based on the dimensionality of the optimization objectives, NSGA-II is applied for the multi-objective beam steering array design, while particle swarm optimization (PSO) is utilized for the single-objective RCS reduction task. This algorithm allocation is determined by the dimensionality of the optimization objectives: NSGA-II handles the multiple target angles of beam steering, whereas PSO efficiently addresses the single-objective uniform scattering problem. The proposed metasurface enables polarization-independent single- and multi-beam steering with arbitrary elevation angles within ±30° and azimuth angles spanning the full 360° range, while the elevation and azimuth angles of individual beams in multi-beam configurations can be independently controlled. In addition, an RCS reduction exceeding 10 dB is achieved over the 0.128–0.710 THz frequency range, corresponding to a fractional bandwidth of 138.90%. Since the optimization procedure is parametric, the framework can be extended to other frequencies. The proposed approach provides a systematic optimization strat-

egy for the design of polarization-independent, reconfigurable, and multifunctional THz coding metasurfaces.

2. Unit Structure Design and Theoretical Analysis

2.1. Unit Structure Design

The structure of the designed topologica- optimization-based coding metasurface unit is shown in Figure 1. It consists of a quartz layer, a polyimide (PI) layer, an LC layer, a metal pattern layer, and a metallic reflective layer. The LC layer is composed of HFUT-HB01 nematic LC, whose molecular orientation can be reoriented under an external bias voltage, resulting in different equivalent permittivity responses. The polyimide layers serve as alignment layers coated on the inner side of the metallic layers, functioning to achieve uniform LC molecular orientation through mechanical rubbing.

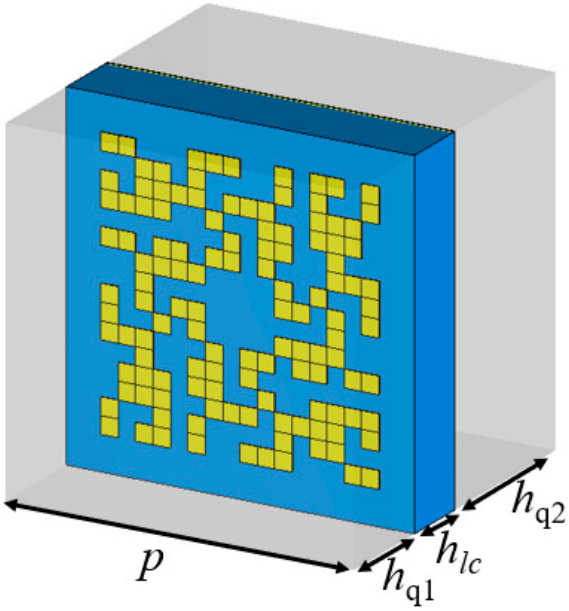

Figure 1. Schematic diagram of the topological optimization-based coding metasurface unit structure. In the metal pattern layer, the yellow squares denote the metal patches, which correspond to the binary state "1", and the blue area denotes the region without metal, which corresponds to "0".

The metal pattern layer is designed using topological optimization, as shown in Figure 2. Taking the center of the metallic pattern as the origin, the surface is divided into four regions with a size of p1 = 40 μm. Each region is further divided into 8 × 8 pixels, where the presence and absence of metal correspond to binary states "1" and "0", respectively. To improve convergence speed and reduce coding complexity, the metallic pattern of Region IV is encoded first, and then the complete metal pattern layer of the unit cell is formed by sequentially rotating the encoded pattern counterclockwise by 90°, 180°, and 270°. The proposed stack is compatible with established liquid-crystal processes: the metal pattern with 5 μm pixels can be defined by electron-beam lithography [12], the polyimide layers are rubbed for alignment [13], the transparent counter-electrode can be formed from ITO nanowhiskers [14,15], and the cell is assembled with glass spacers and filled by vacuum injection [16]; the response can then be characterized by reflection-mode THz-TDS [17]. This rotation-copy constraint is intentionally applied to structurally guarantee polarization independence. It also reduces optimization variables from 256 to 64, accelerating the NSGA-II algorithm. Although the four quadrants are not optimized independently, so that the attainable pattern space is reduced, this is a deliberate trade-off for computational efficiency.

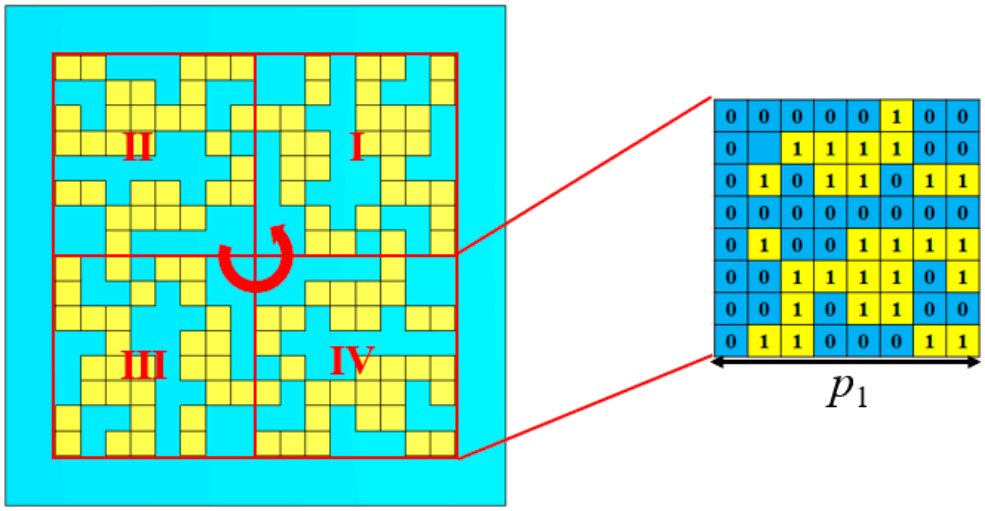

Figure 2. Schematic diagram of the metal pattern layer. Taking the centre of the metallic pattern as the origin, the surface is divided into four regions of size $p_1 = 40$ μm, each further divided into 8 × 8 pixels, where the presence and absence of metal correspond to the binary states "1" and "0", respectively. The inset shows the 0/1 encoding of Region IV; the complete metal pattern layer is formed by sequentially rotating the encoded pattern counterclockwise by 90°, 180° and 270°, as indicated by the arrow.

2.2. Analysis of Theory

The effective dielectric constant of the LC material can be expressed as [18]

$$\varepsilon = \frac{\varepsilon_{\perp}\varepsilon_{\parallel}}{\varepsilon_{\perp}\sin^2\psi + \varepsilon_{\parallel}\cos^2\psi} \tag{1}$$

where ψ is the deflection angle of LC molecules under different bias voltages. $\varepsilon_{\perp}$ is the effective dielectric constant of the LC when no bias voltage is applied, where the long axes of the LC molecules are perpendicular to the direction of the applied electric field. $\varepsilon_{\parallel}$ is the effective dielectric constant of the LC when a saturation bias voltage Vth is applied, where the long axes of the LC molecules are parallel to the direction of the applied electric field. By varying the applied voltage $V_e \in [0, V\text{th}]$, the LC molecules will deflect at different angles, and the dielectric constant of the LC can be continuously adjusted between $\varepsilon_{\perp}$ and $\varepsilon_{\parallel}$. In this paper, the HFUT-HB01 nematic LC is selected. Within the frequency range of 0 THz–2.5 THz when the applied bias voltage is 0 V–10 V, its adjustable range of dielectric constant is 2.47–3.60, and the loss tangent is 0.02.

For the normal incidence of plane waves, the far-field scattering intensity of the coding metasurfaces can be expressed as [19]

$$f(\theta,\varphi) = f_e(\theta,\varphi)\sum_{m=1}^{M}\sum_{n=1}^{N}\exp\left\{-i\left\{\phi(m,n) + KDsin\theta\left[\left(m-\frac{1}{2}\right)\cos\varphi + \left(n-\frac{1}{2}\right)\sin\varphi\right]\right\}\right\} \tag{2}$$

where θ is the elevation angle, φ is the azimuth angle, $f_e(\theta,\varphi)$ is the unit's far-field function, K is the propagation constant, D is the period size of a metasurface unit, and $\phi(m,n)$ is the phase response of the metasurface unit positioned at (m,n) on the metasurface.

Based on the far-field scattering formula of the coding metasurface given by Equation (2), flexible manipulation of electromagnetic waves can be achieved by configuring different phase distributions $\phi(m,n)$ of the unit cells. Therefore, for beam steering, according to the target angle $(\theta_{obj}, \varphi_{obj})$, the phase response $\phi(m,n)$ of the unit is designed to maximize $|f(\theta_{obj}, \varphi_{obj})|$ by using an optimization algorithm. The resulting distribution of $\phi(m,n)$ constitutes the optimal array arrangement of the metasurface for achieving the desired angle control. By employing optimization algorithms to inverse design metasurface array

arrangement, the design efficiency can be enhanced, which enables the manipulation of metasurfaces more proactive and flexible.

3. Results and Discussion

3.1. Topology Optimization Design of Unit Structure

Topological optimization is conducted on the metal pattern layer of the metasurface unit. As described above, the 8 × 8 pixels encoding of Region IV is sequentially rotated counterclockwise three times to form the complete structure. This centrosymmetric pixel arrangement endows the unit cell with polarization-independent characteristics under electromagnetic wave incidence. To further enhance the tunability, the thickness of the LC layer (H_{lc}) and the thickness of the upper quartz layer (H_q) are also incorporated as optimization variables, with their ranges set to 5–85 μm and 8–85 μm, respectively.

In this work, we focus on the inverse design of a 2-bit LC coding unit at a single frequency of 0.56 THz. This specific frequency is chosen to achieve an optimal 90° phase shift based on the available LC dielectric tunability [18,20]. To extend the framework to other THz bands, the new target frequency and the corresponding LC permittivities are set as input parameters, and the structural dimensions are re-optimized automatically; the only constraint is that the LC must still provide a contiguous 2-bit phase range at the new frequency. The effective permittivities of the LC corresponding to the four coding states are set to 2.47, 3.09, 3.24, and 3.60, respectively. Among them, 2.47 and 3.60 correspond to the critical states under zero bias and full bias voltages, while the other two values correspond to intermediate bias states. The optimization involves four conflicting objectives: at the target frequency, the phase differences between adjacent coding states "00/01", "01/10", and "10/11" are all 90°, and the reflection amplitudes of the four states are required to be equal. Conventional single-objective optimization algorithms often deal with such problems by assigning weights to multiple objectives and summing them. However, the choice of weights significantly influences the results, and a balanced solution set cannot be guaranteed. To address this issue, we adopt the NSGA-II multi-objective optimization algorithm in this work. NSGA-II performs a fast non-dominated sorting and retains the best individuals through an elitist strategy, so that a well-distributed Pareto front is obtained in a single run, at the cost of a larger population and more iterations than a single-objective algorithm. The NSGA-II algorithm was configured with a population size of 50, a crossover probability of 0.8, and a mutation probability of 0.05.

In this work, the specific process of using the algorithm to design the metasurface unit inversely is illustrated in Figure 3. First, the optimization parameters for the metasurface unit are initialized: the population size is set to 50, the number of iterations is set to 40, and the fitness function is defined as

$$min = \begin{cases} f_1 = (90 - |p_0 - p_1|)^2 \\ f_2 = (90 - |p_1 - p_2|)^2 \\ f_3 = (90 - |p_2 - p_3|)^2 \\ f_4 = A_{\max} - A_{\min} \end{cases} \quad (3)$$

The optimization objectives are defined as follows. Here, pi ($i = 0, 1, 2, 3$) represent the phase responses of the four coding states of the metasurface unit, A_{max} and A_{min} denote the maximum and minimum reflection coefficients among the four states, respectively. The objectives f_1, f_2, f_3, and f_4 are defined as the deviations of the phase differences between adjacent states from 90° and the deviations of the reflection amplitudes from equality. The optimal solution is achieved when all four objectives are simultaneously minimized to zero, indicating that the phase differences between adjacent states are exactly 90° and the reflection amplitudes of the four states are equal.

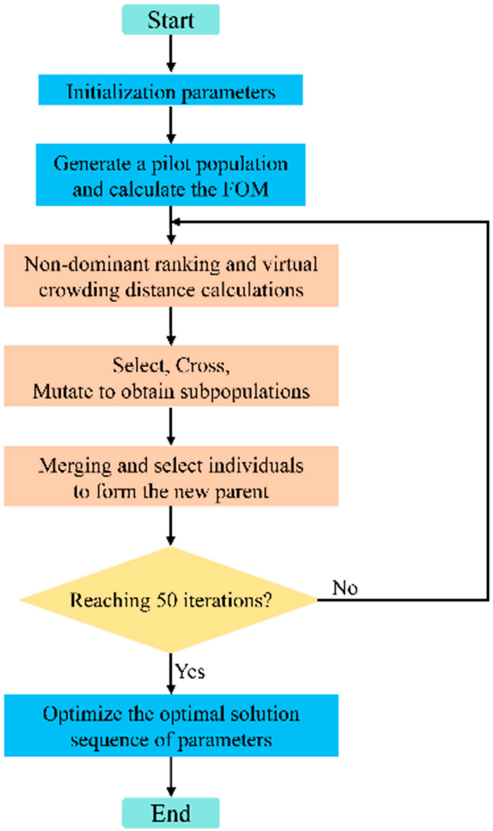

Figure 3. Flow diagram of reverse design metasurface unit based on NSGA-II.

The optimized parameters of the metasurface unit obtained using the NSGA-II muti-objective optimization algorithm are as follows: h_{lc} = 23 μm, h_q = 39 μm. The structure of metal pattern layer is illustrated in Figure 4.

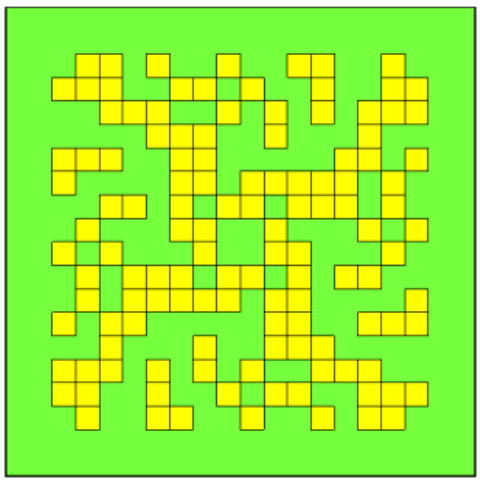

Figure 4. The optimal metal pattern layer obtained by the NSGA-II multi-objective topology optimization. The yellow squares denote metal, corresponding to the binary state "1", and the green area denotes the region without metal, corresponding to "0".

In case of a normally incident plane wave with linear polarization, the metasurface unit is simulated. Figure 5 illustrates the amplitude and phase responses of the metasurface unit at 0.56 THz for transverse electric (TE) and transverse magnetic (TM) mode plane waves. It illustrates that at 0.56 THz, the phase difference between adjacent curves is 90° ± 10°, and the reflection amplitude is greater than 0.55. Furthermore, the responses to TE and TM

mode plane waves are nearly identical. Therefore, the designed coding metasurface unit can achieve polarization-independent 2-bit coding at 0.56 THz.

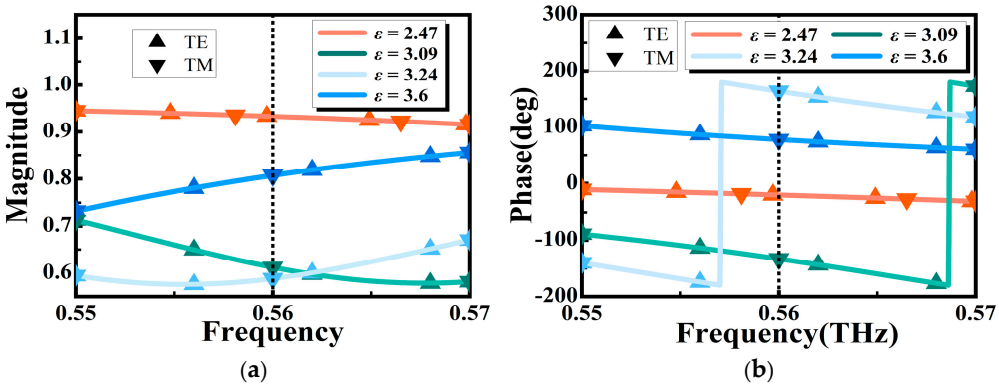

Figure 5. Plots of (**a**) reflection amplitude and (**b**) phase response of the metasurface unit at liquid crystal effective dielectric constants ε of 3.24, 3.6, 2.47, and 3.09, respectively.

To assess the practical feasibility of the topology-optimized unit, its sensitivity to two fabrication imperfections, the pixel dimension and the metal thickness, was analyzed.

First, the pixel size was varied from 5.00 to 4.98 and 5.02 μm, i.e., ±0.4%, which corresponds to the linewidth control of the electron-beam lithography used for patterning. As summarized in Table 1, the maximum phase deviation at 0.56 THz is 5.81°, and the reflection amplitude remains unchanged. Since the coding window is 90° ± 10°, the four coding states remain distinguishable.

Table 1. Phase variations at 0.56 THz caused by pixel dimension errors (±0.02 μm). The ideal 5.0 μm model is taken as the baseline, and Δ represents the absolute difference relative to this baseline.

Pixel Size Error	Parameter	$\varepsilon = 2.47$	$\varepsilon = 3.09$	$\varepsilon = 3.24$	$\varepsilon = 3.6$
−0.4% (4.98 μm)	Δ Phase (°)	0	+4.28	+5.30	+2.61
	Δ Magnitude	0	0	0	0
+0.4% (5.02 μm)	Δ Phase (°)	−0.07	−3.87	−5.81	−2.57
	Δ Magnitude	0	0	0	0

Second, in physical vapor deposition, the thickness tolerance is typically ±10%, so the metal thickness was varied from 0.1 to 0.5 μm. Beyond the skin depth of copper at 0.56 THz (about 0.1 μm) the field no longer penetrates the metal, so the thickness affects neither the reflection coefficient nor the phase; the phase is governed by the geometry of the pattern rather than by the thickness. This was confirmed numerically: because stretching the topological geometry along the z-axis causes severe mesh distortion, the calculation was performed on an equivalent planar sandwich model with the same material parameters, and the phase curves for 0.1, 0.3 and 0.5 μm nearly coincide (Figure 6). Since the pattern geometry is unchanged when the thickness varies, the same insensitivity is expected for the actual structure.

3.2. Analysis of Multifunctional Coding Metasurface Simulation Results

To improve design efficiency and achieve flexible manipulation of terahertz waves, the array arrangement of the coding metasurface is inversely designed using the NSGA-II multi-objective optimization algorithm based on the designed LC coding metasurface unit and the far-field scattering principle of coding metasurfaces. The coding metasurface comprises a 32 × 32 array of coding units. The modeling and simulation of the coding metasurface are performed using CST, with a linearly polarized plane wave as the excitation. The time-

domain solver is adopted, and local mesh refinement is applied to enhance the simulation accuracy. The coding sequences generated by the optimization algorithm are stored on an FPGA board and applied to the array through row and column lines: the 32 × 32 units are connected to 32 row lines and 32 column lines, so that only 64 drive channels are required, while each unit can still be switched independently because the bias across it is the difference between its row and column voltages [21].

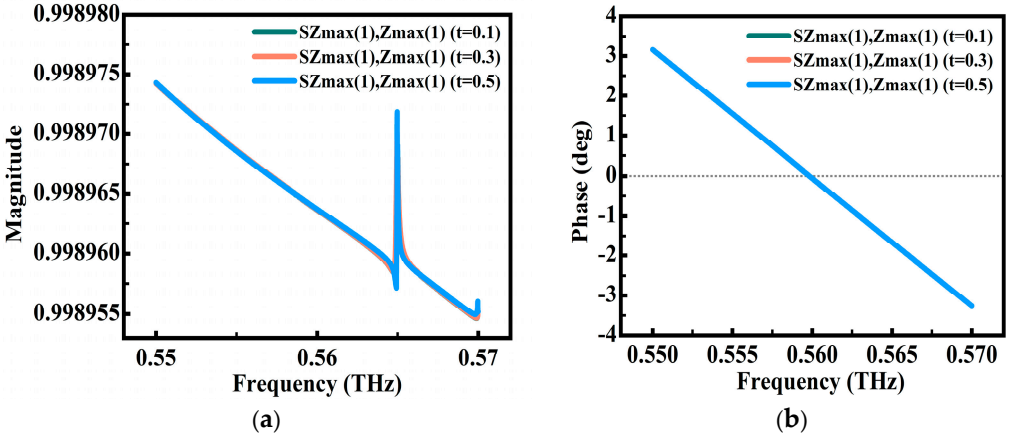

Figure 6. Tolerance analysis of metal thickness variations using an equivalent planar model. (**a**) Reflection phase under different metal thicknesses (0.1 μm, 0.3 μm, 0.5 μm). (**b**) Reflection amplitude under different metal thicknesses. The curves perfectly overlap because the metal thickness significantly exceeds the THz skin depth.

The optimization process for the array arrangements of the metasurface is illustrated in Figure 3. The parameters including the period of the coding unit, the size of the metasurface, and the operating frequency are initialized, and the fitness function is defined as

$$min = \begin{cases} f_1 = |\theta_{r1} - \theta_{ob1}| + |\varphi_{r1} - \varphi_{ob1}| + \dfrac{1}{M-1}\sum_{i=0}^{M} P_{ri} \\ f_2 = |\theta_{r2} - \theta_{ob2}| + |\varphi_{r2} - \varphi_{ob2}| + \dfrac{1}{M-1}\sum_{i=0}^{M} P_{ri} \\ \cdots\cdots \\ f_N = |\theta_{rN} - \theta_{obN}| + |\varphi_{rN} - \varphi_{obN}| + \dfrac{1}{M-1}\sum_{i=0}^{M} P_{ri} \end{cases} \quad (4)$$

where $(\theta_{ob}, \varphi_{ob})$ is the preset target angle, (θ_r, φ_r) is the real angle obtained by simulation, M is the number of beams in the far-field, P_{ri} $(i = 0, 1, \ldots, N)$ is the power of the i-th secondary beam, and N is the number of target beams.

3.2.1. Beam Steering

For the beam steering, to evaluate the error between the simulation results obtained from the reverse design and the preset target, the angle error $E(\theta,\varphi)$ between the actual simulation results and the main lobe of the preset target is defined as follows:

$$E(\theta, \varphi) = \frac{1}{N} \cdot \sum_{i=1}^{N} \frac{1}{2} \cdot \left[\left| \theta_{real} - \theta_{obj} \right| + \left| \varphi_{real} - \varphi_{obj} \right| \right] \quad (5)$$

The beam steering for single-beam and multi-beam $(N = 2, 3, 4)$ at 0.56 THz under different $(\theta_{ob}, \varphi_{ob})$ are studied, and the simulation results are illustrated in Figure 7. Figure 7a–d illustrate the metasurface array arrangements obtained using the NSGA-II algorithm at the target angles, Figure 7e–h illustrate the corresponding three-dimensional far-field scattering results for TE polarization under linearly-polarized plane wave incidence, and Figure 7i–l illustrate the corresponding results for TM polarization.

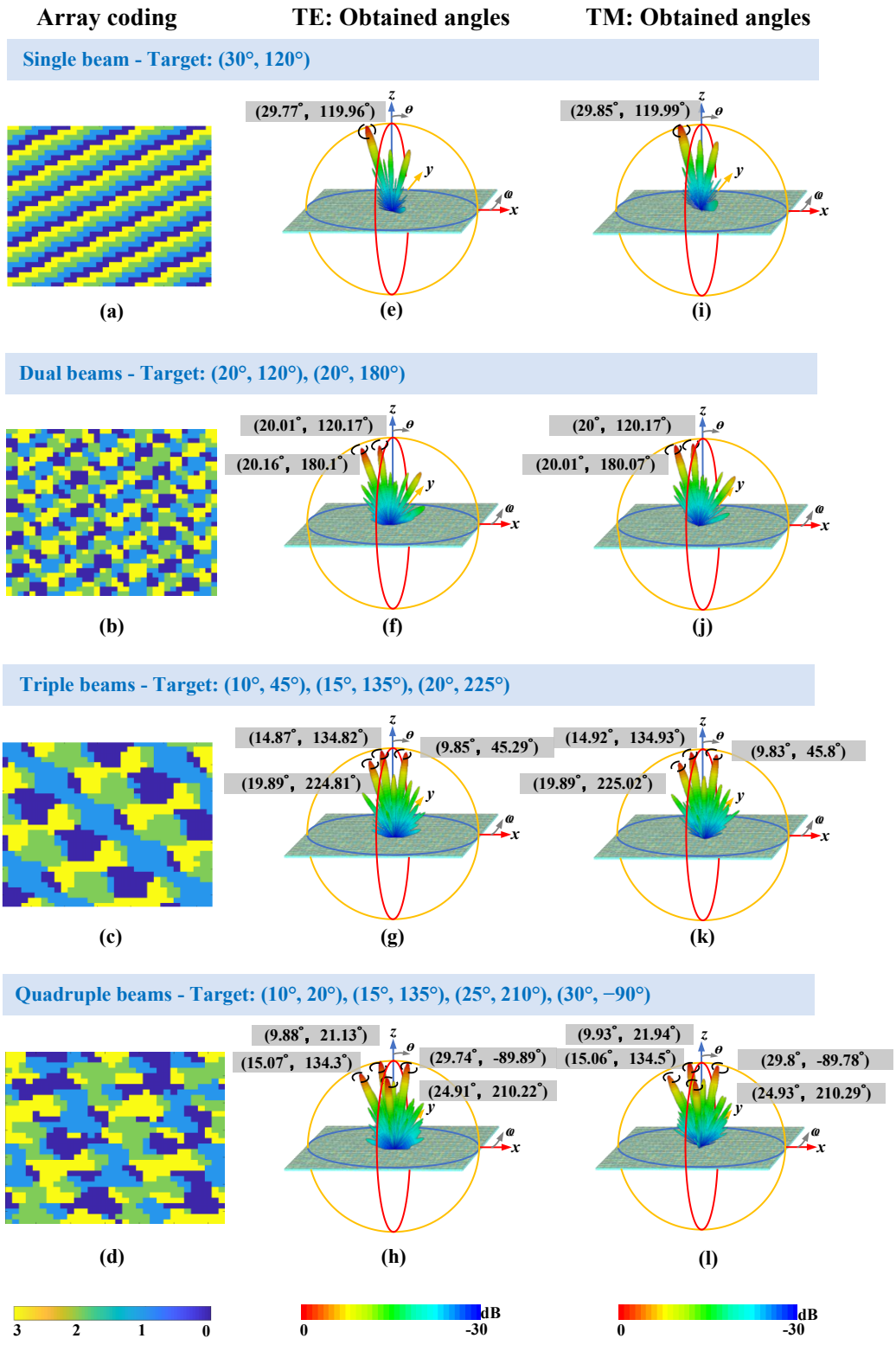

Figure 7. (**a**,**e**,**i**) Array coding sequence and far-field scattering results of (θ_{ob}, φ_{ob}) for single-beam (30°, 120°); (**b**,**f**,**j**) array coding sequence and far-field scattering results of (θ_{ob}, φ_{ob}) for two beams (20°, 120°), (20°, 180°), respectively; (**c**,**g**,**k**) array coding sequence and far-field scattering results of (θ_{ob}, φ_{ob}) for three beams (10°, 45°), (15°, 135°) and (20°, 225°), respectively; (**d**,**h**,**l**) array coding sequence and far-field scattering results of (θ_{ob}, φ_{ob}) for four beams (10°, 20°), (15°, 135°), (25°, 210°) and (30°, −90°), respectively. The color of each pixel in (**a**–**d**) denotes the coding state, as given by the color bar; blue, cyan, green and yellow correspond to the states "00", "01", "10" and "11", respectively.

After calculation, the calculated values of $E(\theta, \varphi)$ for the four cases are 0.14°, 0.11°, 0.18°, and 0.33° for the TE polarization, while they are 0.11°, 0.06°, 0.21°, and 0.42° for the TM polarization, all of which are less than 0.5°. It should be noted that the phase differences between adjacent coding states deviate slightly from the ideal 90° because of the multi-objective trade-off between phase shift and amplitude uniformity. This phase quantization error introduces discontinuities in the phase distribution across the array and excites sidelobes. The differences between the minimum energy of the target beam and the maximum energy of the sidelobes are 5.2 dB, 9 dB, 6.98 dB, and 5.7 dB for the TE polarization, and5.1 dB, 7.9 dB, 6.9 dB, and 5.49 dB for the TM polarization, indicating that the target beam is less affected by sidelobes and the beam steering efficiency is relatively high. In addition, for multi-beam steering, the differences between the highest and lowest scattering amplitudes of the main lobes in the target beam are 0.4 dB, 1.19 dB, and 1.18 dB for the TE polarization, and 0.7 dB, 0.23 dB, and 0.9 dB for the TM polarization, indicating that the energy distribution among the target beams is relatively uniform.

Therefore, the proposed coding metasurface, with its array arrangement inversely designed using the NSGA-II algorithm, can achieve not only multi-beam steering with arbitrary elevation angles within 30° and azimuth angles within 360° at 0.56 THz, but also independent and flexible control of the elevation and azimuth angles of each beam in the multi-beam steering. Compared with the methods that introduce feed compensation phase and utilize complex coding addition theorem to achieve dynamic multi-beam steering, the inverse design approach adopted in this work can improve design efficiency and simplify the design process. Since the proposed metasurface can radiate multiple independent directional beams covering different angular regions on demand, it holds significant potential for applications in multi-input multi-output (MIMO) communication systems, antennas, and radar.

3.2.2. RCS Reduction Performance

In the study of RCS reduction, the particle swarm optimization (PSO) algorithm is employed to effectively improve the optimization efficiency. PSO enables rapid convergence to the optimal solution by simulating swarm-intelligence behavior. Compared with the multi-objective complex computations of NSGA-II, PSO features a simple velocity-position update mechanism and lower computational resource requirements, making it more suitable for RCS design problems with high real-time demands or continuous parameter spaces. As a single-objective algorithm; however, PSO may fall into local optima in highly complex landscapes; for the present problem the objective is a single scalar, and the algorithm converges rapidly to the uniform scattering pattern required for RCS reduction. The flowchart of the coding sequence design based on PSO inverse design is illustrated in Figure 8.

The PSO algorithm is employed to inversely design the array coding of the 2-bit coding metasurface. The coding sequence obtained by PSO inverse design is shown in Figure 9. Firstly, the inversely designed coding array is modeled and simulated in CST to obtain the far-field scattering amplitude. Then, the far-field scattering amplitude of a metal plate with the same size as the coding metasurface is calculated using the same method. Finally, the RCS reduction is obtained by comparing the RCS values of the two.

The RCS reduction is obtained by comparing the RCS of the coding metasurface and the metal plate with the same dimensions, as shown in Figure 10. Figure 10a illustrates the RCS of the 2-bit coding metasurface and the metal plate of the same size, while Figure 10b presents the corresponding RCS reduction. The proposed metasurface achieves over 10 dB RCS reduction across the frequency range of 0.128–0.710 THz, with a fractional bandwidth of 138.90%, and a maximum reduction of 33.12 dB at 0.190 THz. Therefore, the inversely designed 2-bit coding metasurface exhibits excellent performance in RCS reduction.

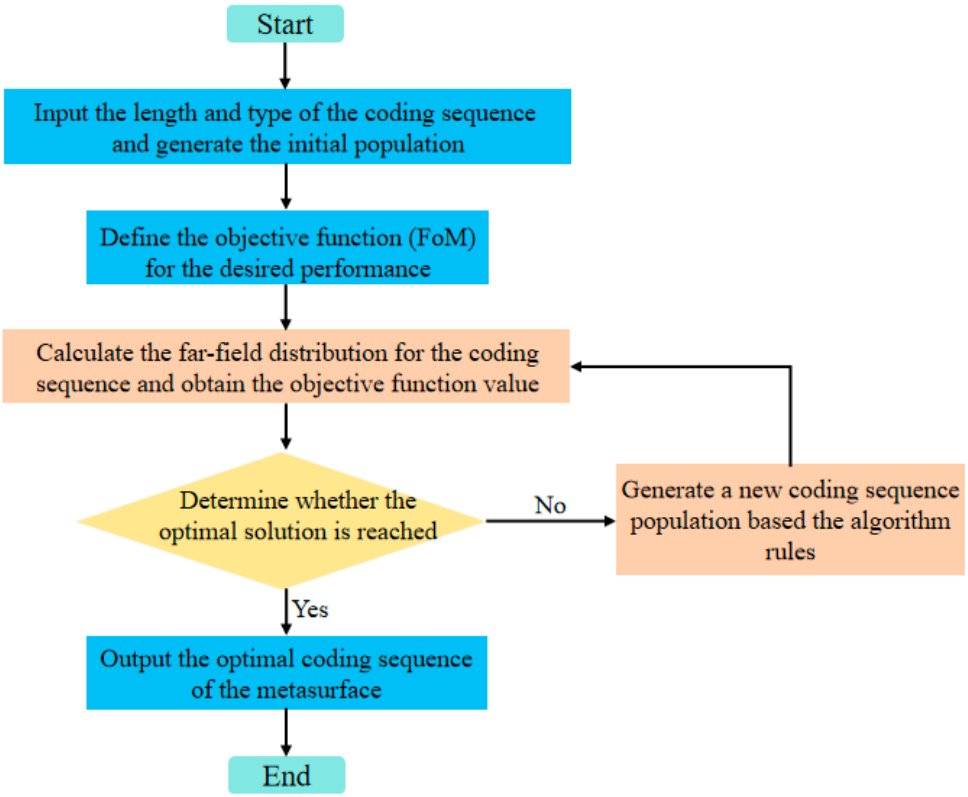

Figure 8. Flowchart of coding sequence design based on PSO inverse design.

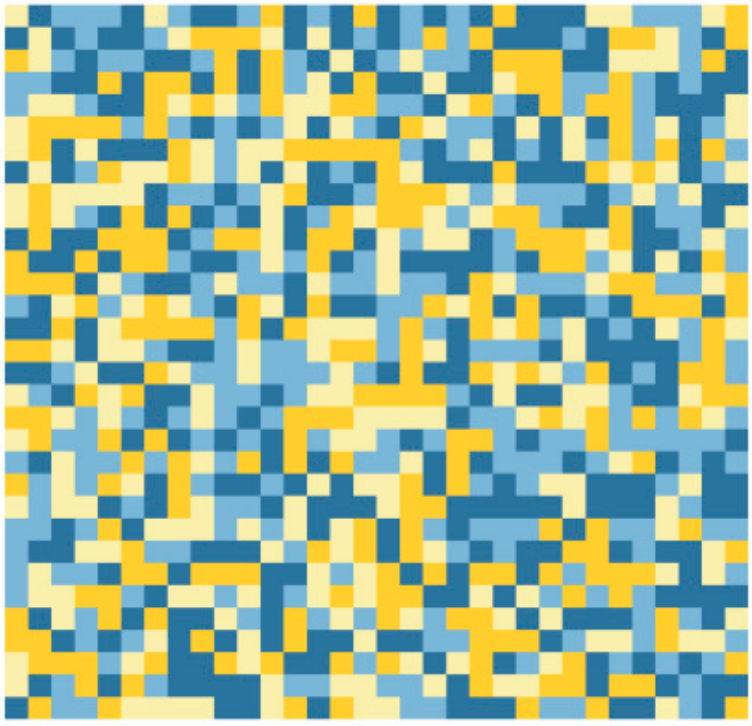

Figure 9. Coding sequence of the metasurface obtained by PSO inverse design. The color of each pixel denotes the coding state of the corresponding unit cell; dark blue, medium blue, light yellow and yellow correspond to the states "00", "01", "10" and "11", respectively.

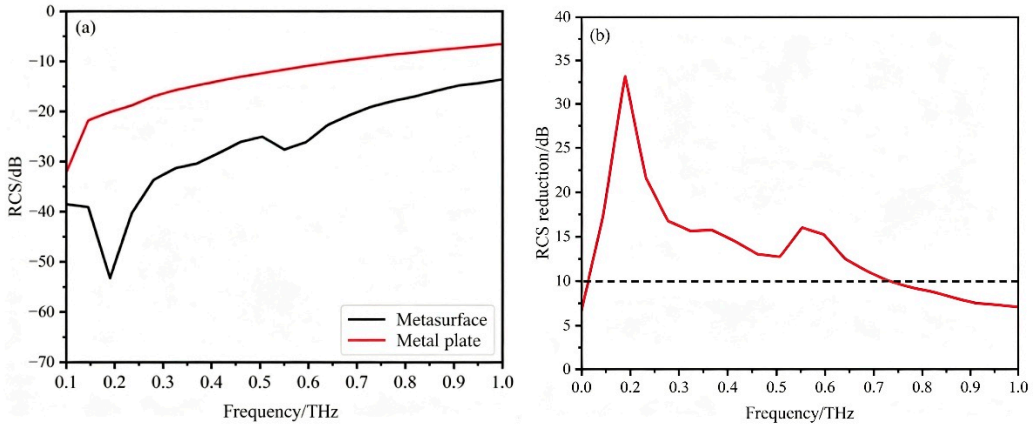

Figure 10. RCS reduction results obtained by inverse design. (**a**) RCS of the coding metasurface and the metal plate with the same dimensions. (**b**) RCS reduction in the metasurface. The dashed line marks the 10 dB level.

Based on the full-wave simulation of the coding metasurface and the metal plate of the same size at 0.190 THz, the results are shown in Figure 10. The inversely designed coding array is modeled and simulated in CST to obtain its far-field scattering pattern, and the results are presented in Figure 11a. Using the same method, the far-field scattering pattern of a metal plate with the same dimensions as the coding metasurface is calculated, as shown in Figure 11b. It can be observed that the metal plate exhibits a strong specular reflection main lobe, while after passing through the coding metasurface, the electromagnetic wave is reflected into multiple directions, generating numerous sidelobes with relatively low energy.

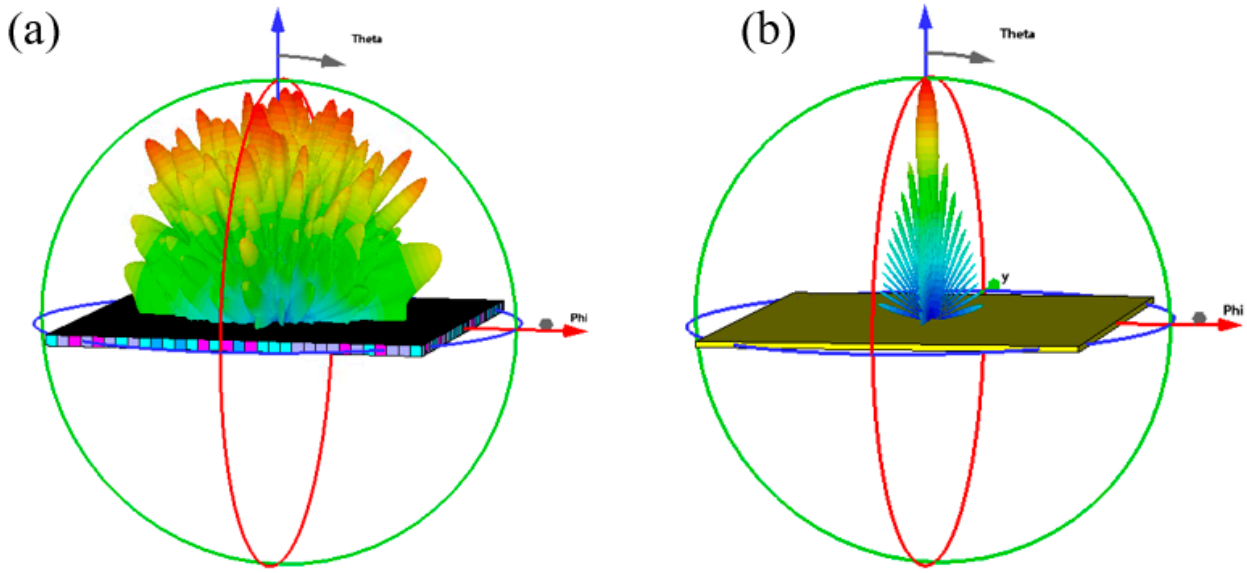

Figure 11. Far-field scattering patterns of (**a**) the coding metasurface and (**b**) a metal plate of the same dimensions. The color denotes the relative scattering intensity, with red representing the highest intensity and blue the lowest; the same scale is used for both subfigures.

Based on the comparison of the far-field scattering performance between the coding metasurface and the metal plate with the same dimensions at 0.190 THz for azimuth angles of $\varphi = 0°$ and $\varphi = 45°$, the results are shown in Figure 11. For $\varphi = 0°$ in Figure 12a, compared with the metal plate, the metasurface suppresses the main lobe energy, and the scattered wave energy at large angles does not increase significantly. For $\varphi = 45°$ in Figure 12b, the RCS at the main lobe is also reduced, while the scattered wave energy at large angles exhibits

a significant enhancement. The results indicate that the metasurface suppresses the main lobe energy and redistributes it uniformly to the sidelobes.

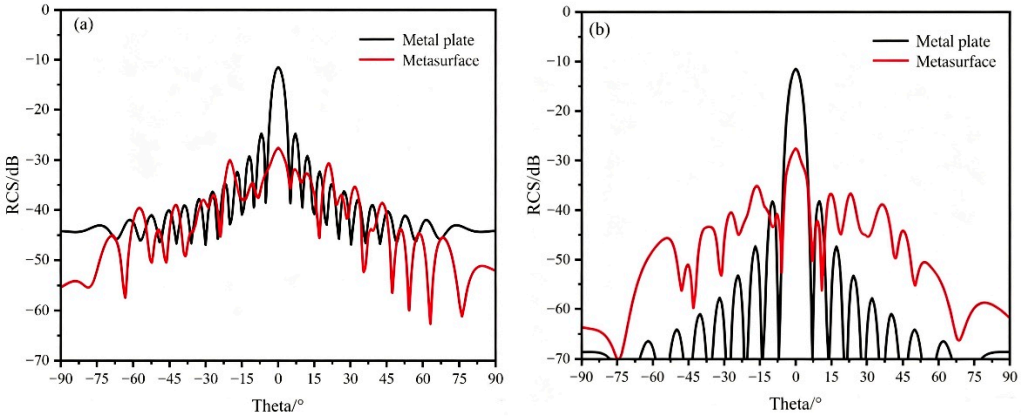

Figure 12. One-dimensional comparison of far-field scattering betweethe coding metasurface and the metal plate with the same dimensions. (**a**) $\varphi = 0°$ (**b**) $\varphi = 45°$.

The RCS reduction performance of the proposed multifunctional metasurface is compared with some previously reported metasurfaces, as summarized in Table 2. The proposed metasurface achieves over 10 dB RCS reduction across the frequency range of 0.128–0.710 THz, with a fractional bandwidth of 138.90% and a maximum reduction of 33.12 dB, along with multifunctional reconfigurability.

Table 2. Comparison of RCS reduction performance with previously reported metasurfaces.

	Coding Type	RCS Reduction Bandwidth	Fractional Bandwidth	Maximum RCS Reduction	Tunable
1	3 bit	2.1–6.9 THz	173%	35 dB	No
2	/	1–10 THz	163%	30 dB	No
3	2 bit	0.7–1.3 THz	60%	25 dB	No
4	1 bit	2.07–3.02 THz 3.78–4.71 THz	37% 22%	/	No
5	3 bit	1–1.4 THz	33%	16 dB	No
6	3 bit	1–1.2 THz	18%	/	No
This work	2 bit	0.128–0.71 THz	138.9%	33.12 dB	Yes

4. Conclusions

In this work, a terahertz 2-bit coding metasurface based on NSGA-II and topological optimization is proposed and investigated. By exploiting the tunable properties of liquid crystal, the programmable control of the metasurface is achieved. The non-dominated sorting genetic algorithm and particle swarm optimization are employed to inversely design the array arrangement of the metasurface, enabling beam steering and RCS reduction functionalities. The results demonstrate that the proposed metasurface achieves 2-bit coding at 0.56 THz, enabling precise control of beam steering with arbitrary elevation angles within ±30° and azimuth angles over 360°, while also achieving over 10 dB RCS reduction with a fractional bandwidth of 138.90% and a maximum reduction of 33.12 dB. This reconfigurable metasurface, realized through inverse design, holds promise for applications in terahertz communication, phased array radar, and vortex radar.

Author Contributions: Conceptualization, C.W., Y.L. and P.L.; methodology, C.W.; software, C.W. and Y.J.; validation, C.W. and J.L.; formal analysis, C.W. and Y.J.; investigation, C.W.; resources, Y.L. and P.L.; data curation, C.W. and J.L.; writing—original draft preparation, C.W.; writing—review and editing, C.W., Y.L. and P.L.; visualization, C.W. and Z.W.; supervision, Y.L. and P.L.; project administration, Y.L. and P.L.; funding acquisition, Y.L. and P.L. All authors have read and agreed to the published version of the manuscript.

Funding: This research was funded by National Natural Science Foundation of China GZ62371248.

Institutional Review Board Statement: Not applicable.

Informed Consent Statement: Not applicable.

Data Availability Statement: The original contributions presented in this study are included in the article. Further inquiries can be directed to the corresponding authors.

Conflicts of Interest: The authors declare no conflict of interest.

References

1. Grade, J.; Haydon, P.; van der Weide, D.W. Electronic terahertz antennas and probes for spectroscopic detection and diagnostics. *Proc. IEEE* **2007**, *95*, 1583–1591. [CrossRef]
2. Zhao, Y.Z.; Huang, C.; Song, Z.L. A digital metamaterial of arbitrary base based on voltage tunable liquid crystal. *IEEE Access* **2019**, *7*, 79671–79676. [CrossRef]
3. Xiao, B.G.; Zhang, Y.; Tong, S.J. Novel tunable graphene-encoded metasurfaces on an uneven substrate for beam-steering in far-field at the terahertz frequencies. *Opt. Express* **2020**, *28*, 7125–7135. [CrossRef] [PubMed]
4. Liu, C.X.; Yang, F.; Fu, X.J.; Wu, J.W.; Zhang, L.; Yang, J.; Cui, T.J. Programmable manipulations of terahertz beams by transmissive digital coding metasurfaces based on liquid crystals. *Adv. Opt. Mater.* **2021**, *9*, 2100932. [CrossRef]
5. Lv, E. Broadband programmable metasurface for multifunctional control of THz waves. In Proceedings of the Conference on Lasers and Electro-Optics (CLEO), San Jose, CA, USA, 7–12May 2023.
6. Zhang, Y.; Ying, K.; Liang, L.; Yao, H.; Yan, X.; Hu, X.; Huang, C.C.; Qiu, F.; Zhang, R.; Li, Y.; et al. Dirac semimetal-enabled multi-bit coding metasurface for dynamic manipulation of terahertz beams. *Curr. Appl. Phys.* **2023**, *53*, 21–27. [CrossRef]
7. Zhang, Y.J.; Luan, J.Q.; Li, C.L.; Chen, Y.; Gao, D.S.; Zhao, M.; Li, P.L. Flexible modulation of terahertz-wave-coded metasurface in thin liquid crystals with topological optimization design. *Acta Opt. Sin.* **2024**, *44*, 1124002.
8. Luan, J.; Zhang, Y.; Chen, Y.; Gao, D.; Li, P.; Li, J. Terahertz multifunctional reconfigurable Dirac semimetal coding metasurface based on genetic algorithm. *Acta Phys. Sin.* **2024**, *73*, 144204. [CrossRef]
9. Han, D.; Ma, Z.Y.; Wang, J.L. Inverse design of metamaterial absorber sensor based on particle swarm optimization. *Chin. J. Lasers* **2022**, *49*, 1714001.
10. Cheng, G.; Si, L.M.; Tang, P.C. Topology optimization of the azimuth-rotation-independent polarization conversion metasurface for bandwidth enhancement. *Opt. Express* **2022**, *30*, 41340–41349. [CrossRef] [PubMed]
11. Zhao, S.D.; Zhang, N.L.; Han, P. Enhanced broadband manipulation of acoustic vortex beams using 3-bit coding metasurfaces through topological optimization. *Small* **2024**, *20*, 2308349. [CrossRef] [PubMed]
12. Chen, H.T.; Padilla, W.J.; Zide, J.M.O.; Gossard, A.C.; Taylor, A.J.; Averitt, R.D. Active terahertz metamaterial devices. *Nature* **2006**, *444*, 597–600. [CrossRef] [PubMed]
13. Nobles, J.E.; Melnyk, O.; Glushchenko, A.; Camley, R.E.; Celinski, Z. Effect of alignment methods on liquid crystal performance in millimeter wave devices. *Eng. Res. Express* **2020**, *2*, 025002. [CrossRef]
14. Yang, C.S.; Tang, T.T.; Pan, R.P.; Yu, P.; Pan, C.L. Liquid crystal terahertz phase shifters with functional indium-tin-oxide nanostructures for biasing and alignment. *Appl. Phys. Lett.* **2014**, *104*, 141106. [CrossRef]
15. Yang, C.S.; Tang, T.T.; Chen, P.H.; Pan, R.P.; Yu, P.; Pan, C.L. Voltage-controlled liquid-crystal terahertz phase shifter with indium-tin-oxide nanowhiskers as transparent electrodes. *Opt. Lett.* **2014**, *39*, 2511–2514. [CrossRef] [PubMed]
16. Wang, L.; Xiao, R.W.; Ge, S.J.; Shen, Z.X.; Lü, P.; Hu, W.; Lu, Y.Q. Research progress of terahertz liquid crystal materials and devices. *Acta Phys. Sin.* **2019**, *68*, 084205. [CrossRef]
17. Grischkowsky, D.; Keiding, S.; van Exter, M.; Fattinger, C. Far-infrared time-domain spectroscopy with terahertz beams of dielectrics and semiconductors. *J. Opt. Soc. Am. B* **1990**, *7*, 2006–2015. [CrossRef]
18. Chen, Y.; Cao, W.H.; Li, J.Q.; Zhang, M.Z.; Du, X.Y.; Gao, D.S.; Li, P.L. Broadband polarization-independent terahertz multifunctional liquid crystal coding metasurface based on topological optimization. *Chin. Phys. B* **2025**, *34*, 044205. [CrossRef]
19. Cui, T.J.; Qi, M.Q.; Wan, X. Coding metamaterials, digital metamaterials and programmable metamaterials. *Light Sci. Appl.* **2014**, *3*, e218. [CrossRef]

20. Gao, S.; Yang, J.; Wang, P.; Zheng, A.; Lu, H.; Deng, G.; Lai, W.; Yin, Z. Tunable liquid crystal based phase shifter with a slot unit cell for reconfigurable reflectarrays in F-band. *Appl. Sci.* **2018**, *8*, 2528. [CrossRef]
21. Zhu, W.; Wang, S.; Guo, H.; Tian, D.; Wang, L.; Xu, Y.; Wan, F.; Cui, H.; Huang, X.; Wu, J.; et al. High-contrast transmissive terahertz programmable metasurface based on liquid crystal. *ACS Photonics* **2025**, *12*, 3892–3900. [CrossRef]

Disclaimer/Publisher's Note: The statements, opinions and data contained in all publications are solely those of the individual author(s) and contributor(s) and not of MDPI and/or the editor(s). MDPI and/or the editor(s) disclaim responsibility for any injury to people or property resulting from any ideas, methods, instructions or products referred to in the content.